Theory of Chemical Bonds in Metalloenzymes I: Analytical and Hybrid-DFT Studies on Oxo and Hydroxo Diiron Cores

M. SHOJI, Y. NISHIYAMA, Y. MARUNO, K. KOIZUMI, Y. KITAGAWA, S. YAMANAKA, T. KAWAKAMI, M. OKUMURA, K. YAMAGUCHI

Department of Chemistry, Graduate School of Science, Osaka University, Toyonaka, Osaka 560-0043, Japan

ABSTRACT: Oxo- or hydroxo-bridged diiron centers are ubiquitous in metalloenzymes such as hemerythrin (Hr), ribonucleotide reductase, methane monooxygenase, and rubrerythrin. In each enzyme the diiron core plays a central role in the highly specific reaction. To elucidate mechanisms of these reactions, many experimental studies have been carried out, and bioinorganic model compounds have also been synthesized for the purpose. In this study electronic structures of diiron centers for Hr model compounds are investigated from the viewpoint of magnetic interactions. To this end, the Hubbard model for the three-center four-electron bond is analytically solved to elucidate an important role of electron correlation and the resulting superexchange interaction between localized spins. The hybrid density functional theory (DFT) calculations also are performed for Hr model compounds to provide the natural orbitals and their occupation numbers, which are crucial for computations of several chemical indices, such as effective bond order, information entropy, and unpaired electron density. These indices are useful for characterization and understanding of chemical bonds in FeOFe cores. The calculated effective exchange integrals (J_{ab}) are wholly consistent with the available experiments. The orbital interactions in the FeOFe cores are reconsidered in relation to recent work by other groups. It is found that magnetic interactions are sensitive to the hydrogen bonds in the systems and are related to effective regulation of the activity. Implications of the

Correspondence to: M. Shoji; e-mail: mshoji@chem.sci.osaka-u.ac.jp

calculated results are discussed in relation to the nature of chemical bonds in the FeOFe cores of several biological systems.   © 2004 Wiley Periodicals, Inc. Int J Quantum Chem 100: 887–906, 2004

Introduction

Hemerythrin (Hr) exists as oxygen transport protein in marine invertebrate phyla [1]. This protein is able to bind oxygen reversibly. Hemerythrin contains a binuclear iron center, where two irons are bridged by a hydroxide and two carboxylates in the deoxyHr. The latter groups are part of aspartic and glutamic acid residues. Other coordination ligands in the Hr diiron center are five histidine side chains and oxygen from molecular oxygen. In the oxy or met Hr Fe^{3+} ion is in the highest-spin (HS) state and the HS Fe^{2+} ion is involved in the deoxyHr. In the process of oxygen binding, the hydrogen atom moves from oxygen of hydroxide to peroxo anion and μ-oxo bridge is generated in oxyHr. This change of bridging ligand affects the magnetic properties of the diiron center. Diiron centers exhibit antiferromagnetic coupling as $J = -13$ cm^{-1} in deoxyHr and $J = -77$ cm^{-1} in oxyHr, respectively, where J is the exchange coupling constant in the Heisenberg model [2]. Thus, the magnitude of J is sensitive to oxidation state of diiron core in Hr and related species.

The oxo- or hydroxo-bridged diiron centers are ubiquitous in metalloenzymes such as Hr, ribonucleotide reductase, methane monooxygenase, and rubrerythrin. In these enzymes the diiron core has an important part to play in the highly specific reactions. To elucidate and utilize these reactions, many model compounds have been synthesized, and experimental studies for structural, spectroscopic, and magnetic properties have been carried out [3, 4]. For example, tribridged μ-oxo diiron structures are realized in [Fe$_2$(O)(O$_2$CCH$_3$)$_2$(HBpz$_3$)$_2$] (**1**) and [Fe(O)(O$_2$CCH$_3$)$_2$(Me$_3$TACN)$_2$]$^{2+}$ (**2**) [5, 6]. Compounds **1** and **2** have been extensively studied in comparison with metalloproteins by spectroscopic [7, 8], structural [9–15], and magnetic [6, 16, 17] techniques. Both complexes have shown the reversible protonation ability at the μ-oxo center, and **2** has a two-electron reduction property in consort with the protonation as Hr [16, 17]. Other model complexes for nonheme iron proteins are [Fe(OAc)(HB(3,5-iPr2pz)3)] and its derivatives, which have five-coordinated ferrous [18].

Generally, theoretical studies of chemical bonds in transition-metal oxides are not difficult because of the necessity of appropriate treatment of strong electron correlation and spin correlation effects. As a typical example, we consider oxygen-carrying proteins, such as hemoglobin and hemocyanin. Hemoglobins and myoglobins are found in all vertebrates and most invertebrates. Hemocyanins are found in various arthropods and mollusks. Myoglobins and hemoglobins are heme-containing proteins and hemocyanins have dicopper sites. Myoglobins and myohemerythrins are oxygen store proteins in muscle tissue. The Fe(II)O$_2$ cores in hemoglobin and myoglobin are singlet, although molecular oxygen is triplet in the ground state. Therefore, the singlet state of the Fe(II)O$_2$ cores is regarded as the triplet-coupled singlet state $^1[^3Fe(II)^3O_2]$ or doublet-coupled singlet state $^1[^2Fe(III)^2O_2^-]$ and/or their mixed state [1, 2, 19]. Similar electron-transfer reactions are also known for the [Cu(I)$_2$ + ^{3}O$_2$] core in hemocyanines [1, 2, 20]. Thus, the singlet state under consideration is not a simple closed-shell state but an exchange-coupled singlet state of open-shell species. From this picture, active sites of oxygen-transport proteins are nothing but strong electron-correlated systems [21] with or without temperature-dependent paramagnetism. Thus, theoretical investigation of the nature of chemical bonds in metalloenzymes is an important and interesting problem in quantum chemistry.

In past decades we investigated several three-center systems with open-shell characters: R$_2$COO, MOO (M=Fe, Mn), MO, and MOM (M=Cr, Mn, Co, Fe, Ni, Cu) on the basis of both broken-symmetry (BS) and symmetry-adapted (SA) methods [22–26]. The BS spin unrestricted Hartree–Fock (UHF) calculations have been performed to elucidate electronic structures of these species, diradical character, and spin density populations. The SA complete active space (CAS) configuration interaction (CI) by the use of the natural orbitals (UNO) of the UHF solutions also are performed, to calculate the excitation energies and singlet–triplet energy gap (2J) of the species. The effective exchange integral (J) in the

Heisenberg model also is calculated, using both BS and SA methods [21–26]

$$H = -2J_{ab}\mathbf{S_a} \cdot \mathbf{S_b}, \qquad (1)$$

where $\mathbf{S_c}$ denotes the spin at site c. Comparisons between BS and SA calculations of J have been carried out to examine the reliability of the former approach. However, examples examined previously [20, 24] have been limited to small model systems instead of real systems. Fortunately, recent development of BS density functional methods enable us to perform first-principle calculations of realistic transition-metal oxides [27].

In this study, we first consider an important role of electron correlation for μ-oxo– or μ-hydroxo–bridged diiron core on the basis of the Hubbard model. A spin-polarized orbital picture is derived from the CI analysis, leading to a theoretical model for superexchange coupling between Fe ions. The hybrid density functional theory (HDFT) calculations are performed for μ-oxo– or μ-hydroxo–bridged diiron systems as the realistic Hr model complexes. The natural orbital (NO) analysis of the spin-polarized DFT solutions also is conducted, to elucidate the shape of NOs and their occupation numbers, which are used to define several chemical indices, such as effective bond order and information entropy. The effective exchange integrals are calculated using the total energies of DFT solutions, and major superexchange interaction pathways are determined by NO analysis. It is found that the exchange interaction drastically decreases through protonation of the μ-oxo core, and the dioxygen binding mechanisms of the Hr are complicated with the coupling between charge transfer and proton-transfer beyond simple electrostatic interactions [1, 2, 25]. The clarification of magnetic interactions between diirons is important and interesting not just for μ-oxo– or μ-hydroxo–bridged diiron systems but also for elucidation of esoteric dioxygen binding process in Hr. Finally, implications of the current theoretical results are discussed in relation to reliability of HDFT theory for elucidation of the nature of chemical bonds in diiron cores of enzymes.

Theoretical Backgrounds

HUBBARD MODELS FOR TRANSITION METAL OXIDES

The Huckel model often breaks down for transition-metal complexes with strongly and intermedi-ary correlated electron systems [21]. The extended Hubbard Hamiltonian [28–30] can be generally used for such systems

$$H = H_q + H_d + H_{pd}, \qquad (2)$$

where H_q denotes the Hamiltonian for $p(\pi)$- or d-electron, and H_{pd} is the interaction Hamiltonian between them as follows:

$$H_q = \sum T_{qq}a_q^+ a_q + \sum U_{qp}a_q^+ a_q b_r^+ b_r (q, r = p \text{ or } d)$$

$$H_{pd} = \sum T_{pd}(a_p^+ b_d + a_d^+ b_p), \qquad (3)$$

where a^+ and b^+ create electron (or hole) on the i-th a site and the j-th b site, respectively. Variables U_{aa} and U_{ab} ($=V$) are on-site and intersite Coulomb repulsions, and T_{aa} ($=\varepsilon_{aa}$) and T_{ab} are orbital energy and transfer integral between $p(\pi)$- and d-orbitals, respectively. The parameters used in Eq. (3) were estimated from the ab initio DFT calculations [31–33] and spectroscopic data [34]. The charge transfer (CT) excitation energy (Δ_{pd}) from hydrooxo anion or oxygen dianion to the d-vacant orbital is given under the Hubbard model as

$$\Delta_{pd} = (\varepsilon_{dd} - \varepsilon_{pp}) + (U_{dd} - U_{pp}) \cong (\varepsilon_{dd} + U_{dd}) - \varepsilon_{pp}, \qquad (4)$$

where U_{pp} and U_{pd} are neglected for simplicity. The Δ_{pd} value remains positive even if $\varepsilon_{dd} < \varepsilon_{pp} < 0$, because U_{dd} is largely positive for transition-metal ions.

The transition-metal oxides are classified from the relative magnitude of U_{dd} and Δ_{pd} into three types [28–30]: (a) CT insulator ($\Delta_{pd} < U_{dd}$), (b) intermediate case ($\Delta_{pd} \cong U_{dd}$), and (c) Mott–Hubbard insulator ($\Delta_{pd} > U_{dd}$). Judging from the calculated results by hybrid DFT, the diiron cores in Hr and related species are regarded as the CT insulator. The CT excitation energy should play an important role in the diiron cores, as illustrated in Figure 1.

HUCKEL–HUBBARD MODEL FOR DIIRON CORES

The Fe ion in diiron cores Fe(X)YFe(X) (X = II, III) has five or four unpaired d-electrons, which interact with oxygen dianion or hydrooxo anion (Y = O^{2-}, OH^{1-}). Therefore, the effective exchange interaction between Fe ions arises mainly from the
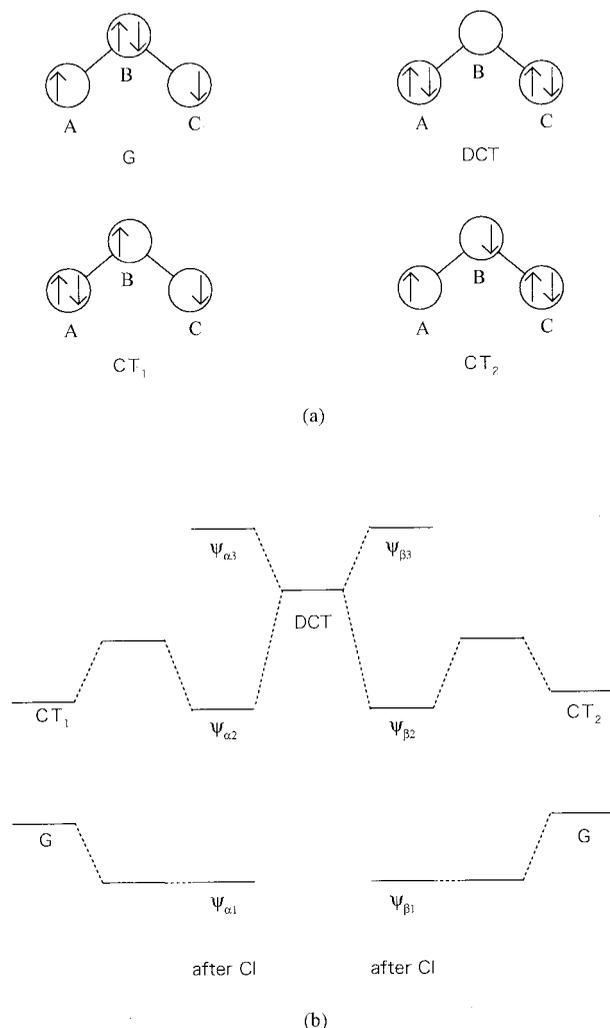
FIGURE 1. (a) Spin-dependent ground (G), charge-transfer (CT), and double charge transfer (DCT) configurations for the VB CI calculations. (b) Spin-polarized orbital energy diagrams obtained by the VB CI calculations.

superexchange interaction via the bridging ligand. In fact, the electronic structure for each d-orbital symmetry is regarded as the three-orbital four-electron (3,4) system. The exact diagonalization (full CI) [28–30] of singlet and triplet CI matrices for the Hubbard model provide the effective exchange integral in Eq. (1) as

$$E_{CI}(\text{singlet}) - E_{CI}(\text{triplet}) = 2J_{dd}. \quad (5)$$

On the other hand, the effective exchange integral [Eq. (5)] between iron d-orbital is approximately given by the perturbation theory as

$$J_{dd} = -\frac{2T_{pd}^4}{\Delta_{pd}}\left\{\frac{1}{\Delta_{pd}^2} + \frac{1}{U_{dd}\Delta_{pd}}\right\} = -2(t_{dd})^2\left\{\frac{1}{\Delta_{pd}} + \frac{1}{U_{dd}}\right\}$$

$$(6a)$$

$$= \frac{-2(t_{dd})^2}{\Delta_{pd}}\left(t_{dd} = \frac{T_{pd}^2}{\Delta_{pd}}\right). \quad (6b)$$

From Eq. (6a), J_{dd} is sensitive to the magnitude of Δ_{pd} and U_{dd}. Its magnitude increases sharply with the decrease of Δ_{pd}, as in the case of CT insulator, and it is approximately given by Eq. (6b) if the contribution of CT between Fe ions in Eq. (6a) is neglected.

From Eq. (4), the magnitude of Δ_{pd} is variable with the d-orbital energy, which is sensitive to the oxidation state of Fe(X) ion. The Δ_{pd} value for Fe(III) is smaller than that of Fe(II), because ε_{dd} for Fe(III) $< \varepsilon_{dd}$ for Fe(II) < 0. This in turn indicates the tendency, $|J_{dd}|$ for Fe(III) $> |J_{dd}|$ for Fe(II), which is consistent with the experiments [1–5]. In fact, J-values for deoxy Hr(Fe(II)), oxy Hr (Fe(III)) with the OOH anion, and met Hr(Fe(III)) are -13, -77, and -134 cm^{-1}, respectively. The hydrogen bonding between μ-oxo and HOO anion in the oxy Hr reduces the electron-donating property of O^{2-} to Fe(III), suppressing the superexchange interaction. Thus, the general tendency in antiferromagnetic exchange interactions in diiron cores is explained by the perturbation theory. However, if the Fe ion has a higher oxidation state (X $>$ III), Δ_{pd} becomes too small to violate the perturbation theory [Eq. (6b)]. Alternately, the variational treatment is essential in the situation [29].

ORBITAL INTERACTIONS THROUGH BRIDGING LIGAND

There are two variational approaches to binuclear transition-metal oxides. One is the molecular orbital (MO) approach, whereas the other is the valence bond (VB) approach. Here, the latter is used as s starting point to obtain the spin-polarized picture in the spin-unrestricted DFT calculations. For the VB description, the localized orbitals for the left and right Fe ions are referred to as A and C, respectively, whereas the bridging ligand is named as B. Here, it is assumed that A site has an α spin and C site has a β spin. Site B has ligand orbitals, which are occupied by one α electron and one β electron. Figure 1a illustrates possible VB-type configurations: the ground (G), CT between Fe ion and ligand
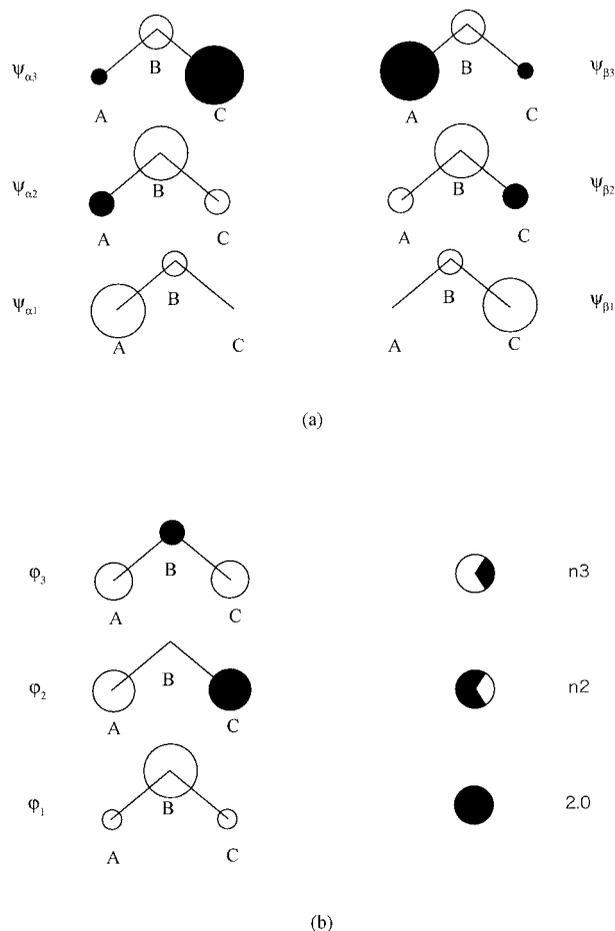
(a)

(b)

FIGURE 2. (a) Schematic illustrations of three spin-polarized MOs for each spin obtained by the VB CI calculations in Figure 1 and spin-polarized UHF or UDFT calculations. (b) Three NOs and their occupation numbers for 3,4 systems obtained by the diagonalization of the spinless first-order reduced density matrix by the VB CI, UHF, and UDFT.

anion, and double charge transfer (DCT) between them [25].

The orbital mixing between A and B sites or between C and B sites occurs because of the CI between G and CT configurations (see Fig. 1b), giving the following spin-polarized bonding orbitals as illustrated in Figure 2a,

$$\Psi_{\alpha 1} = \cos\theta_1 a_{A\uparrow}^\dagger + \sin\theta_1 a_{B\uparrow}^\dagger, \qquad (7a)$$

$$\Psi_{\beta 1} = \cos\theta_1 a_{C\downarrow}^\dagger + \sin\theta_1 a_{B\downarrow}^\dagger, \qquad (7b)$$

where the mixing parameter θ_1 is determined by the bonding parameter (T_{pd}) and the energy gap Δ_{pd}

between G and CT. On the other hand, the destabilized antibonding orbitals ($\Psi_{\alpha 1}^*$, $\Psi_{\beta 1}^*$) are stabilized by CI between CT and DCT, leading to the second occupied MOs, as shown in Figure 2a

$$\Psi_{\alpha 2} = \cos\theta_2(-\sin\theta_1 a_{A\uparrow}^\dagger + \cos\theta_1 a_{B\uparrow}^\dagger) + \sin\theta_2 a_{C\uparrow}^\dagger, \qquad (7c)$$

$$\Psi_{\beta 2} = \cos\theta_2(-\sin\theta_1 a_{C\downarrow}^\dagger + \cos\theta_1 a_{B\downarrow}^\dagger) + \sin\theta_2 a_{A\downarrow}^\uparrow, \qquad (7d)$$

where θ_2 is determined by T_{pd} and the energy gap between CT and DCT. Similarly, virtual orbital $\varphi_{\alpha 3}$ ($\varphi_{\beta 3}$) is determined from orthonormalization to occupied orbitals as $\Psi_{\alpha 1}$ ($\Psi_{\beta 1}$) and $\Psi_{\alpha 2}$ ($\Psi_{\beta 2}$)

$$\Psi_{\alpha 3} = -\sin\theta_2(-\sin\theta_1 a_{A\uparrow}^\dagger + \cos\theta_1 a_{B\uparrow}^\dagger) + \cos\theta_2 a_{C\uparrow}^\dagger \qquad (7e)$$

$$\Psi_{\beta 3} = -\sin\theta_2(-\sin\theta_1 a_{C\downarrow}^\dagger + \cos\theta_1 a_{B\downarrow}^\dagger) + \cos\theta_2 a_{A\downarrow}^\dagger. \qquad (7f)$$

The three orbitals for each spin are schematically illustrated in Figure 2a. They are nothing but spin-polarized orbitals obtained by the UHF and UDFT methods. As shown below, the orbital mixing parameters θ_1 and θ_2 for Hr model compounds are determined by these calculations.

SYMMETRY-ADAPTED ORBITALS VIA SPIN-POLARIZED ORBITALS

As shown above, the spin-polarized orbitals result from CI among the G, CT, and DCT configurations in Figure 1, where the origin of spin polarization is responsible for strong electron correlation effect via on-site Coulomb repulsion (U_{dd}) [see Eq. (4)]. Because the spin-polarized orbitals usually are symmetry-broken, they often are transformed to symmetry-adapted orbitals, referred to as NO, as shown in Figure 2b. For this purpose, all-electron wavefunction $a_{\alpha 1}^\dagger a_{\alpha 2}^\dagger a_{\beta 1}^\dagger a_{\beta 2}^\dagger$ is used to construct the spinless first-order reduced density matrix, which is diagonalized as [21, 35]

$$\rho(x, x') = \sum_i n_i \varphi_i(x)\varphi_i^*(x'). \qquad (8)$$

Then, the natural orbital φ_i is an eigen vector of ρ, and its eigen values n_i correspond to occupation

numbers. The NOs for the 3,4 bond are symmetry-adapted, as illustrated in Figure 3.

The relative stability between symmetric (S) and antisymmetric (A) NOs depends on the symmetry of the localized orbitals on the B site as follows

$$\varphi_1 = \cos \omega_1 a_B^\dagger + \sin \omega_1 \frac{1}{\sqrt{2}} (a_A^\dagger + a_C^\dagger), \quad (9a)$$

$$\varphi_2 = \frac{1}{\sqrt{2}} (a_A^\dagger \mp a_C^\dagger), \quad (9b)$$

$$\varphi_3 = -\sin \omega_1 a_B^\dagger + \cos \omega_1 \frac{1}{\sqrt{2}} (a_A^\dagger \pm a_C^\dagger), \quad (9c)$$

where ω_1 depends on θ_1 and θ_2. The S- or A-type NO becomes the most stable, depending on the symmetry of a_B orbital. The orbital interaction schemes [21] are explained on the basis of the SA picture as shown in Figures 3a and 3b.

The occupation number is an important factor to diagnose the nature of the chemical bond [21]. It is expressed analytically by

$$n_1 = 2.0, \quad (10a)$$

$$n_2 = 1 + (\cos^2\theta_1\sin^2\theta_2 + 2 \sin \theta_1\cos 2\theta_2)$$
$$= 1 + \cos 2\omega_2, \quad (10b)$$

$$n_3 = 1 - (\cos^2\theta_1\sin^2\theta_2 + 2 \sin \theta_1\cos 2\theta_2)$$
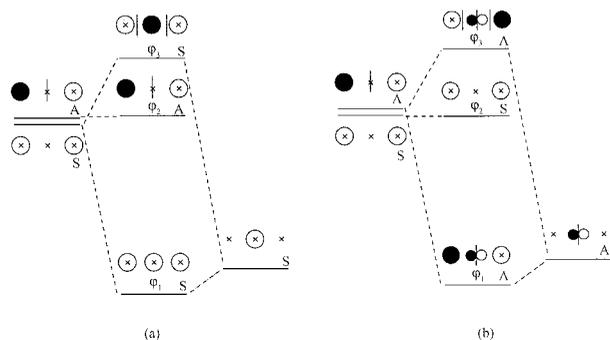$$= 1 - \cos 2\omega_2. \quad (10c)$$

FIGURE 3. Orbital interaction schemes between SA orbital of the terminal atomic pair and the orbital of the central bridging atom. (a) The bridging orbital is symmetric about the center. (b) The bridging orbital is asymmetric about the center. The orbital splitting patterns are different between the (a) and (b) cases.
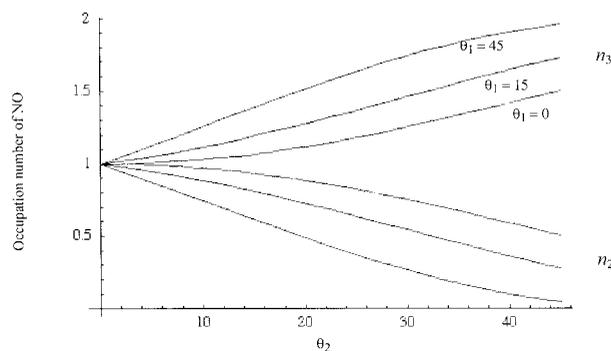

FIGURE 4. Variations of the occupation numbers of the second and third NOs for 3,4 systems with change of the orbital mixing parameter θ_2(degree) at the three typical states of the other orbital mixing parameter θ_1(degree).

The magnitude of n_i is variable, depending on the orbital interaction parameters ($0 \leq \theta_1 \leq \pi/4$, $0 \leq \theta_2 \leq \pi/4$). Figure 4 illustrates variations of n_i with θ_2, assuming that $\theta_1 = 0°$, 15°, and 30°. From Figure 4, n_2 increases with the increase of the spin delocalization degree θ_2 on bridging ligand. As delocalization θ_1 of d-orbitals on Fe ions becomes increasingly larger, n_2 increases sharply with θ_2. In consequence, n_2 increases when interactions between d-orbital on Fe ion and bridging ligand orbital are strong. Because θ_1 and θ_2 are closely related to the orbital energy, transfer energy, and on-site Coulomb energy in Eqs. (3) and (5), the nature of the 3,4 bonds is determined by them. For quantitative analysis, UHF and hybrid UDFT computations are necessary to determine the θ_1 and θ_2 or ω_1 and ω_2 parameters for real diiron systems.

Spin-Polarized DFT Calculations

BROKEN SYMMETRY AND APPROXIMATE SPIN PROJECTION METHOD

The DFT method has opened possibilities to calculate large molecules such as proteins. Particularly, BS methodology provides a practical procedure to involve nondynamical correlations in transition-metal cores of enzymes and can give reasonable potential curves of metal–metal bonds like CAS–self-consistent field (SCF). The first-order density matrix by DFT is diagonalized as shown in Eq. (8) to obtain the symmetry-adapted NO, which are often referred to as density functional theory natural orbital (DNO) [31–33, 35]. The natural spin or-

bitals for the 3,4 systems are often spin-polarized because of strong electron correlation as

$$\phi_{1\alpha} = \phi_{1\beta} = \varphi_1, \qquad (11a)$$

$$\phi_{2\alpha} = \cos \omega_2 \varphi_2 + \sin \omega_2 \varphi_3, \qquad (11b)$$

$$\phi_{2\beta} = \cos \omega_2 \varphi_2 - \sin \omega_2 \varphi_3, \qquad (11c)$$

where α and β denote the up- and down-spin, respectively. The corresponding orbitals ($\phi_{2\alpha}$ and $\phi_{2\beta}$) obtained by the bonding and antibonding NO pairs are different from the canonical spin-polarized orbitals in Eq. (7) [36, 37]. They are lucid for pictorial understanding of the orbital interactions because of the strong orthogonality [21]. The occupation numbers of the second and third NOs are given by the orbital mixing parameter ω_2 as expressed by Eq. (11), whereas ω_1 is used to determine the shapes of NOs.

However, the BS calculations entail spin contamination arising from higher energy states, and a projection method is necessary to purify the spin state [21]. One way of doing projection is to use approximate spin projection (AP) method. The AP method approximately removes triplet configuration term in the BS singlet state. The four-electron wavefunctions for three-center systems are given by

$$\Psi = |\varphi_1\bar{\varphi}_1\phi_{2\alpha}\bar{\phi}_{2\beta}| = \cos^2\omega_2|\varphi_1\bar{\varphi}_1\varphi_2\bar{\varphi}_2|$$

$$- \sin^2\omega_2|\varphi_1\bar{\varphi}_1\varphi_3\bar{\varphi}_3| + \frac{1}{2}\sin 2\omega_2(|\varphi_1\bar{\varphi}_1\varphi_2\bar{\varphi}_3|$$

$$|\varphi_1\bar{\varphi}_1\varphi_2\bar{\varphi}_3|). \quad (12)$$

The third term of Eq. (12) corresponds to the triplet configuration term. The AP wavefunction is obtained by eliminating this term as

$$\Psi^{AP} = \frac{1}{\sqrt{\cos^4\omega_2 + \sin^4\omega_2}}(\cos^2\omega_2|\varphi_1\bar{\varphi}_1\varphi_2\bar{\varphi}_2|$$

$$- \sin^2\omega_2|\varphi_1\bar{\varphi}_1\varphi_3\bar{\varphi}_3|). \quad (13)$$

With this projection in wavefunction the occupation numbers are projected easily. From Eq. (11), the orbital overlap of BS orbitals is defined by

$$T = \langle\phi_{2\alpha}|\phi_{2\beta}\rangle = \cos 2\omega_2. \qquad (14)$$

The spin-polarized orbitals of BS solution and the NOs have the following relations,

$$\varphi_{\pm} = \frac{1}{\sqrt{2(1 \pm T)}}(\phi_{2\alpha} \pm \phi_{2\beta}), \qquad (15a)$$

$$n_{\pm} = 1 \pm T, \qquad (15b)$$

where φ_+ has bonding orbital nature and φ_- does antibonding orbital one for superexchange interaction. With regard to the section titled "Symmetry-Adapted Orbitals via Spin-Polarized Orbitals," the NO analysis provides the following relations: $\varphi_+ = \varphi_2$, $\varphi_- = \varphi_3$ and the orbital overlap $T = \cos^2\theta_1\sin^2\theta_2 + 2\sin\theta_1\cos 2\theta_2$ in Eq. (10). The occupation number n is also projected to $n_{\pm}^{AP}$ by the AP procedure as follows

$$n_{\pm}^{AP} = \frac{4n_{\pm}^2}{4 + (n_+ - n_-)^2}. \qquad (16)$$

CHEMICAL INDICES

Natural orbitals reflect the symmetry of molecule, which is a key issue for symmetry-adapted CAS-SCF methods. The CAS-SCF calculations are desirable but are not as easy for large molecules. Therefore, NOs given by diagonalization of the first-order density matrix by UHF or hybrid unrestricted density functional theory (UDFT) are useful as an alternative to CAS-SCF orbitals to elucidate bonding natures on the basis of the symmetry-adapted orbitals. In fact, chemical indices [38, 39] derived from the occupation numbers enable us to perform quantitative analysis of chemical bonds.

The effective bond order b is defined as the difference between the occupation numbers of the bonding and antibonding natural orbitals

$$b = \frac{n_+ - n_-}{2} = T, \qquad (17a)$$

where b is 1.0 for the closed-shell ($T = 1.0$) and 0.0 for the complete diradical. The b is equal to the orbital overlap T between spin-polarized orbitals in Eq. (14). The effective bond order B after spin projection is defined by

$$B = \frac{(n_+^{AP} - n_-^{AP})}{2} = \frac{2T}{1 + T^2}. \qquad (17b)$$

The B-value is always larger than the b-value because $T \leq 1.0$.

The Jaynes information entropy is also defined to express the characteristic of chemical bonds with fractional occupation numbers n_i as shown in Figure 2b by

$$I = -n_i \ln n_i. \qquad (18a)$$

The normalized Jaynes information entropy is defined by setting the maximum binding state $I_c = -2 \ln 2$ as the reference, as

$$I_n = \frac{I_c - I}{I_c}. \qquad (18b)$$

The diradical character Y is defined by the weight of doubly excited configuration (W_D) as

$$Y = 2W_D = 1 - \frac{2T}{1 + T^2} = \frac{n^2 - 4n + 4}{n^2 - 2n + 2}, \qquad (19)$$

where Y is equal to $1 - B$.

If spin-polarized orbitals in Eq. (11) exist near a strong bonding region, both effective bond order and information entropy are almost equal to 1. Therefore, the delocalized MO picture in Eq. (11) provides a good starting point for theoretical description of the transition-metal–oxygen bonds. On the other hand, spin-polarized orbitals near the dissociation limit are almost localized on transition-metal ions, and the b and I_n values are almost zero. Spin densities appear in this region, and the spin-dependent picture is useful for understanding the nature of chemical bonds. The spin density Q is described by the occupation number n_i under the BS approximation [21] as

$$Q = \sqrt{1 - T_i^2} = \sqrt{1 - (n_i - 1)^2} = \sqrt{n_i(2 - n_i)}. \qquad (20)$$

Because the spin density should be zero in the singlet state, the unpaired electron density U is alternately defined as the deviation of total spin angular momentum from the exact singlet value as

$$U = n_i(2 - n_i) = Q^2. \qquad (21)$$

These chemical indices are acceptable for characterization of chemical bonds in transition-metal oxides.

UHF AND HYBRID DFT COMPUTATIONS

Electron correlation effects for transition-metal oxides are often intermediate. This implies that theoretical investigations from both strong and weak correlation sides are desirable for these species. Therefore, UHF, HDFT (UBHandHLYP and UB3LYP) and pure DFT (UBLYP) calculations are performed to obtain total energies of the lowest spin (LS) and HS states, and NOs and their occupation numbers. Becke's three-parameter hybrid functional [40] using the Becke exchange functional [41] and the LYP correlation functional [42] is abbreviated as B3LYP. The abbreviation BHandH LYP has half of the Becke 88 exchange functional. Exchange-correlation forms in the hybrid DFT method are generally defined by

$$E_{XC} = C_1 E_X^{HF} + C_2 E_X^{Slater} + C_3 \Delta E_X^{Becke88}$$
$$+ C_4 E_C^{VWN} + C_5 \Delta E_C^{LYP}. \qquad (22)$$

The parameter sets C1, C2, C3, C4, and C5 are 0.5, 0.5, 0.5, 1.0, and 1.0 for BHandHLYP and 0.2, 0.8, 0.72, 1.0, and 0.81 for B3LYP, respectively. All the calculations were performed with Gaussian 98 program package [43]. The basis sets 6-31G* given by Hariharan et al. [44] and Pople et al. [45] were used for hydrogen, boron, carbon, nitrogen, and oxygen atoms. Huzinaga MIDI [46] basis plus Hay's diffuse [47] basis sets were used for iron atoms.

As shown previously, the on-site Coulomb repulsion U_{dd} in Eq. (2) can be estimated by using the calculated J_{ab} values and transfer integrals (T_{pd}). The magnitude of U_{dd} is approximately expressed by the scaled value as

$$U_{dd}(\text{Hybrid DFT}) = U_{dd}(\text{UHF}) f(w), \qquad (23)$$

where f is the scaling function and w is the fraction of the UHF exchange functional. The f values are 1.0 for UHF and 0.0 for Huckel model, whereas they remain nonzero but smaller than 1.0 for hybrid DFT. The general tendency is as follows;

$$U_{dd}(\text{UHF}) > U_{dd}(\text{BHandHLYP})$$
$$> U_{dd}(\text{B3LYP}) > U_{dd}(\text{BLYP}). \qquad (24)$$

Then, the magnitude of J_{ab} values in Eqs. (1) and (5) should exhibit the reverse tendency of that of Eq. (24).

The BS UHF and UDFT methods are applicable to estimate J_{ab} values in Eq. (1). To this end, three

expressions of J values, $J_{ab}^{(1)}$ [48–50], $J_{ab}^{(2)}$ [51], and $J_{ab}^{(3)}$ [24, 52, 53], have been proposed as

$$J_{ab}^{(1)} = \frac{{}^{LS}E_X - {}^{HS}E_X}{S_{max}^2}, \qquad (25a)$$

$$J_{ab}^{(2)} = \frac{{}^{LS}E_X - {}^{HS}E_X}{S_{max}(S_{max} + 1)}, \qquad (25b)$$

$$J_{ab}^{(3)} = \frac{{}^{LS}E_X - {}^{HS}E_X}{{}^{HS}\langle S^2 \rangle_X - {}^{LS}\langle S^2 \rangle_X}, \qquad (25c)$$

where S_{max} denotes the size of spin in the HS state and ${}^{Y}\langle S^2 \rangle_X$ is the total spin angular momentum for the spin state Y (HS or LS state) obtained by the computational method X. Variable $J_{ab}^{(3)}$ is estimated from the AP procedure described by Eq. (13) and can be equally applicable to both spin SA and BS methods. On the other hand, the others (25a) and (25b) are applicable only to the BS method.

The effective exchange integrals have been determined experimentally for diiron cores in metalloenzymes [1–5]. We can use these magnetic parameters for examination of the reliability of the hybrid DFT calculations in Eq. (22). In fact, UB3LYP is found to give reasonable results compared with available experiments on the species. The NO analysis of the four different hybrid DFT solutions have been performed to obtain the chemical indices. This in turn indicates the characteristic features of them. The full-geometry optimizations of the diiron complexes have not been performed here. Alternately, their geometries were taken from databases described in the next section.

X-Ray Structures and Computational Geometries

COORDINATE DATA OF MODEL COMPOUNDS

(A) *Model 1: (μ-oxo)bis(μ-acetate)bis[hydrotris(1-pyrazolyl)borato]diiron(III), [Fe$_2$(O)(O$_2$CCH$_3$)$_2$-(HBpz$_3$)$_2$] (**1a**)*

All the geometrical coordinates of component atoms were taken from the X-ray structure data in the Cambridge Structural Database (CSD) [54] (CDS code of CACZIP10) [55]. The structure of [Fe$_2$(O)(O$_2$CCH$_3$)$_2$(HBpz$_3$)$_2$] is shown in Figure 5A.
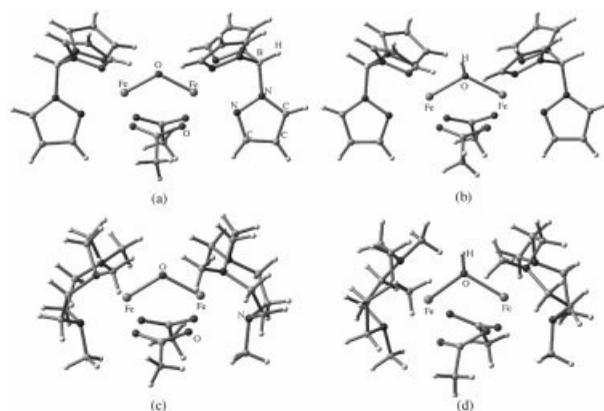
FIGURE 5. Geometrical structures of diiron complexes obtained by X-ray analysis: (a) [Fe$_2$O(O$_2$CCH$_3$)$_2$(HBpz$_3$)$_2$] (**1a**), (b) [Fe$_2$OH(O$_2$CCH$_3$)$_2$(HBpz$_3$)$_x$]$^+$ (**1b**), (c) [Fe$_2$O(O$_2$CCH$_3$)$_2$(Me$_3$TACN)$_2$]$^{2+}$ (**2a**), and (d) [Fe$_2$OH(O$_2$CCH$_3$)$_2$(Me$_3$TACN)$_2$]$^+$ (**2b**).

(B) *Model 2: (μ-hydroxo)bis(μ-acetate)bis[hydrotris(1-pyrazolyl)borato]diiron(III), [Fe$_2$(OH)(O$_2$CCH$_3$)$_2$(HBpz$_3$)$_2$] (**1b**)*

All the position coordinates of component atoms were taken from the X-ray structure data (CDS code of COCJIN) [15]. The structure of [Fe$_2$(OH)(O$_2$CCH$_3$)$_2$(HBpz$_3$)$_2$]$^+$ is shown in Figure 5B.

(C) *Model 3: (μ-oxo)bis(μ-acetate)bis[1,4,7-trimethyl-1,4,7triazacyclononane]diiron(III), [Fe$_2$(O)(O$_2$CCH$_3$)$_2$(Me$_3$TACN)$_2$]$^{2+}$ (**2a**)*

All the position coordinates of nonhydrogen atoms were taken from the X-ray structure data of DIBXAN10 [6]. In this data, positions of all the hydrogen atoms were not reported. Geometrical information of some ethyl hydrogen atoms of Me$_3$TACNs and one side of methyl hydrogen atoms of acetate were lost. The positions of hydrogen atoms were determined using the geometries of the next ethyl-hydrogens in Me$_3$TACN and methyl in acetate. The structure of [Fe$_2$(O)(O$_2$CCH$_3$)$_2$(Me$_3$TACN)$_2$]$^{2+}$ is shown in Figure 5C.

(D) *Model 4: (μ-hydroxo)bis(μ-acetate)bis[1,4,7-trimethyl-1,4,7 triazacyclononane]diiron(II), [Fe$_2$(OH)(O$_2$CCH$_3$)$_2$(Me$_3$TACN)$_2$]$^+$ (**2b**)*

All the position coordinates of nonhydrogen atoms were taken from the X-ray structure data (CDS

code of DIBWUG10) [6]. In this data, positions of the μ-hydroxo hydrogen atom were not reported. Two X-ray structure data of similar complexes having μ-hydroxo diiron(II) center were found out over CDS. They are (μ-hydroxo)-bis(μ-triphenylethanoato)-bis(1,4,7-triazacyclononame)-diiron tetraphenyl borate acetonitrile solvate (**3**) [56] and (μ-hydroxo)-bis((m-trifluoroacetato-0,0′)-(1,4,7-trimethyl-1.4.7-triazacyclononane-N,N,N))-diiron trifluoromethanesulfonate(**4**) [57]. In **3** (CDS code of TUQJUK) the bond length between hydrogen and oxygen of μ-hydroxo is 0.624, and the bond angle of iron-oxygen-hydrogen is 117.3°. In **4** (CDS code of PEXZUN) the bond length between hydrogen and oxygen of μ-hydroxo is 0.872, and the bond angle of iron-oxygen-hydrogen is 119°. Model **4** has a longer O—H bond length than does **3** for the hydrogen bonding to counter anion, which exists above the μ-hydroxo. The counter anion in **3** is located on the side of Me$_3$TACN. In this calculation hydrogen geometry of former compound was adopted for μ-hydroxo bridge. The structure of [Fe$_2$(OH)(O$_2$CCH$_3$)$_2$-(Me$_3$TACN)$_2$]$^+$ (**2b**) is shown in Figure 5D.

Computational Results

ORBITAL INTERACTIONS

The Fe ions in systems considered in this study have five or four unpaired spins. In conformity with the linear 3,4 system in Figure 3, we first consider the five d-p-d conjugated orbitals for the linear Fe-O-Fe system.

$$\sigma\{dz^2(A),\ pz(B),\ dz^2(C)\}\ (A),\quad (26a)$$

$$\pi_1\{dxz(A),\ px(B),\ dxz(C)\}\ (S),\quad (26b)$$

$$\pi_2\{dyz(A),\ py(B),\ dyz(C)\}\ (S),\quad (26c)$$

$$\delta_1\{dx^2-y^2((A),\ L,\ dx^2-y^2)(C)\}\ (S),\quad (26d)$$

$$\delta_2\{dxy((A),\ L,\ dxy)(C)\}\ (S),\quad (26e)$$

where S and A in the last parentheses denote symmetric and antisymmetric, respectively. The subindex 1 indicates that orbital has reflective symmetry of the mirror plane including two irons and bridging oxygen atoms. The local coordinates are defined in each iron site as Z-axis directs to μ-oxo and the mirror is ZX plane. In this definition, the δ-orbitals
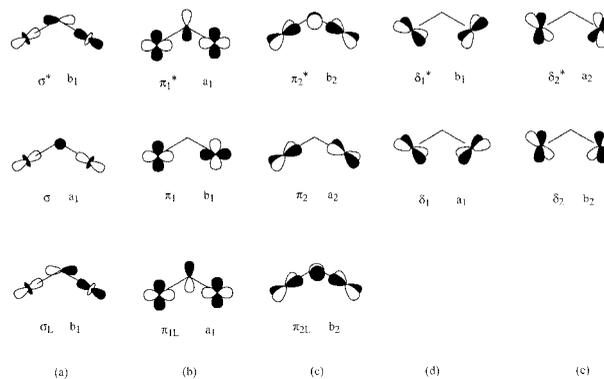

FIGURE 6. Schematic representations of NOs for d-p-d conjugated systems: (a) σ-type interaction through p_x orbital; (b) π_1-type interaction through p_z orbital; (c) π_2-type interaction through p_y orbital (orbital symmetries are named on the assumption that each molecule has quasi-C$_{2V}$-symmetric structure), (d) δ_1-type and δ_2-type. These d-orbitals have no interaction through the bridging ligand.

interact with ligand (L) orbitals except for the central O atom B.

Next we consider the bent [Fe$_2$O(OOCR$_2$)$_2$] cores in **1** and **2**. If orbital interactions through oxo bridge are focused on, they have quasi-C$_{2\nu}$ symmetry despite coordination ligands, (OOCR$_2$)$_2$, are little out of symmetry. Symmetry group C$_{2\nu}$ has a_1, a_2, b_1, and b_2 symmetry elements. Instead of the x-axis in the linear FeOFe system, the C$_2$-axis of [Fe$_2$O(OOCR$_2$)$_2$] cores was taken to be the Z-axis and the X-axis was taken through two iron atoms. The mirror plane in the bent [Fe$_2$O(OOCR$_2$)$_2$] core is equal to the ZX plane. As discussed in the second section, there are three NOs—NO1, NO2, and NO3—for the core, in order of the higher occupation numbers. Because Fe ions have large on-site coulomb repulsion, NO1 is made up of a majority of bridging ligand orbital and NO2 and NO3 are made up of spin-site orbitals for the most part.

The σ-type orbital interaction is feasible through p_x orbital on μ-oxo in the bent cores. The p_x orbital is antisymmetric (b_1) on the mirror operation for the YZ plane. The symmetries of σ-type orbitals are therefore b_1, a_1, and b_1 for NO1 (σ_L), NO2 (σ), and NO3 (σ^*), respectively, as shown in Figure 6a. The 2s and p_z orbitals on μ-oxo come to be mixed into σ orbital. The π_1-type orbital interaction is obtained through p_z orbital with a_1 symmetry on μ-oxo, although p_x also participates. The symmetries of π_1-type orbitals are a_1, b_1, and a_1 for NO1 (π_{1L}), NO2 (π_1), and NO3 (π_1^*), respectively, as illustrated in

TABLE I

Chemical indices of the NOs for Hr model compounds 1 (1a).[a]

Methods	Orbital interaction	b	I	B	Y	Q	U
UHF	σ	0.0905	0.0682	0.1796	0.8204	0.9959	0.9918
	$\pi 1$	0.0726	0.0542	0.1444	0.8556	0.9974	0.9947
	$\pi 2$	0.0626	0.0466	0.1248	0.8752	0.9980	0.9961
	$\delta 1$	0.0066	0.0048	0.0133	0.9867	1.0000	1.0000
	$\delta 2$	0.0064	0.0046	0.0127	0.9873	1.0000	1.0000
UBHandHLYP	σ	0.1896	0.1490	0.3661	0.6339	0.9819	0.9640
	$\pi 1$	0.1698	0.1324	0.3301	0.6699	0.9855	0.9712
	$\pi 2$	0.1496	0.1156	0.2926	0.7074	0.9887	0.9776
	$\delta 1$	0.0192	0.0140	0.0383	0.9617	0.9998	0.9996
	$\delta 2$	0.0180	0.0131	0.0360	0.9640	0.9998	0.9997
UB3LYP	σ	0.3392	0.2822	0.6084	0.3916	0.9407	0.8849
	$\pi 1$	0.3201	0.2645	0.5807	0.4193	0.9474	0.8975
	$\pi 2$	0.2454	0.1971	0.4629	0.5371	0.9694	0.9398
	$\delta 1$	0.0450	0.0332	0.0899	0.9101	0.9990	0.9980
	$\delta 2$	0.0373	0.0274	0.0744	0.9256	0.9993	0.9986
UBLYP	σ	0.7574	0.7148	0.9626	0.0374	0.6529	0.4263
	$\pi 1$	0.7300	0.6840	0.9525	0.0475	0.6834	0.4671
	$\pi 2$	0.3869	0.3272	0.6731	0.3269	0.9221	0.8503
	$\delta 1$	0.1094	0.0831	0.2162	0.7838	0.9940	0.9880
	$\delta 2$	0.0693	0.0517	0.1379	0.8621	0.9976	0.9952

[a] Antiferromagnetic spin state.

Figure 6b. While, π_2-type orbital interaction is through p_y orbital with a_2 symmetry on μ-oxo. The symmetries of π_2-type orbitals are b_2, a_2, and b_2 for NO1 (π_{2L}), NO2 (π_2) and NO3 (π_2^*), respectively (see Fig. 6c). Among NOs of σ, π_1, and π_2, only σ orbital has different symmetry (A). This difference of nodes appears as the sign of resonance parameter B, as shown in Figure 3. The δ-type orbitals exhibit negligible interactions with μ-oxo. The δ-type orbital interactions are through ligands that are orthogonally oriented to μ-oxo. These are carboxyl groups in acetic acids for the Hr model complexes. The symmetries of these orbitals are shown in Figure 6d.

NATURAL ORBITAL ANALYSIS AND ITS OCCUPATION NUMBERS

General Tendencies of Chemical Indices

The spin-polarized UHF and DFT (UBHandH-LYP, UB3LYP, and BLYP) calculations have been performed for four complexes **1a–2b**. The NOs and their occupation numbers are also determined using the LS singlet solutions. The chemical indices defined in the third section are calculated using the occupation numbers obtained by the four methods. The calculated results are summarized in Tables I through IV. From these tables, the orbital overlap T and effective bond order b ($T = b$) are largely dependent on the computational methods, particularly for the cases of σ and π orbitals. For example, the b values of the σ orbital of the model 1 (**1a**) are 0.091 and 0.757 by UHF and pure DFT(BLYP), respectively. This is consistent with the general tendency that UHF underestimates the bonding character, whereas BLYP overestimates it for transition-metal oxides. On the other hand, the corresponding values by UBHandHLYP and UB3LYP are 0.392 and 0.634, respectively. Thus, the T and b values are sensitive to the weight (w) of HF exchange potential in the hybrid DFT method.

The b and B value for σ orbital decreases with the weight ($w = x$) of the HF exchange potential and is approximately expressed by

$$T = b \cong p \exp(-qx), \qquad (27a)$$

$$B = \frac{2p \exp(-qx)}{1 + p^2 \exp(-2qx)}, \qquad (27b)$$

SHOJI ET AL.

TABLE II

Chemical indices of the NOs for Hr model compound 2 (1b).[a]

Methods	Orbital interaction	b	I	B	Y	Q	U
UHF	σ	0.0381	0.0280	0.0761	0.9239	0.9993	0.9985
	$\pi 2$	0.0134	0.0097	0.0267	0.9733	0.9999	0.9998
	$\delta 1$	0.0094	0.0068	0.0188	0.9812	1.0000	0.9999
	$\delta 2$	0.0087	0.0063	0.0173	0.9827	1.0000	0.9999
	$\pi 1$	0.0073	0.0053	0.0146	0.9854	1.0000	0.9999
UBHandHLYP	σ	0.0888	0.0668	0.1762	0.8238	0.9960	0.9921
	$\pi 2$	0.0316	0.0231	0.0631	0.9369	0.9995	0.9990
	$\delta 1$	0.0255	0.0186	0.0509	0.9491	0.9997	0.9994
	$\delta 2$	0.0227	0.0165	0.0453	0.9547	0.9997	0.9995
	$\pi 1$	0.0172	0.0125	0.0343	0.9657	0.9999	0.9997
UB3LYP	σ	0.1741	0.1359	0.3379	0.6621	0.9847	0.9697
	$\pi 2$	0.0645	0.0480	0.1285	0.8715	0.9979	0.9958
	$\delta 1$	0.0535	0.0396	0.1067	0.8933	0.9986	0.9971
	$\delta 2$	0.0480	0.0354	0.0957	0.9043	0.9988	0.9977
	$\pi 1$	0.0373	0.0274	0.0746	0.9254	0.9993	0.9986
UBLYP	σ	0.5293	0.4687	0.8270	0.1730	0.8484	0.7198
	$\pi 2$	0.2808	0.2287	0.5206	0.4794	0.9598	0.9211
	$\delta 1$	0.1345	0.1033	0.2642	0.7358	0.9909	0.9819
	$\delta 2$	0.1068	0.0810	0.2113	0.7887	0.9943	0.9886
	$\pi 1$	0.0671	0.0500	0.1336	0.8664	0.9977	0.9955

[a] Antiferromagnetic spin state.

where p and q are fitting parameters, summarized in Table V. Similarly, the normalized information entropy I_n is also expressed by two parameters as

$$I_n \cong 1 - p \exp(-qx). \quad (27c)$$

On the other hand, the diradical character Y increases with the increase of w, and it can be expressed by using Eqs. (19) and (27a) as

$$Y = 1 - \frac{2T}{1 + T^2} \cong \frac{\{1 - p \exp(-qx)\}^2}{1 + p^2\exp(-2qx)}. \quad (27d)$$

Similarly, unpaired electron density U and spin density Q increase with w and are defined by using Eqs. (20), (21), and (27a) as

$$U = 1 - T^2 \cong 1 - p^2\exp(-2qx), \quad (27e)$$

$$Q = \sqrt{1 - T^2} \cong \sqrt{1 - p^2\exp(-2qx)}. \quad (27f)$$

The effective exchange integrals in the Heisenberg model is approximately given by Eq. (6b) as

$$J = -\frac{t_{dd}^2}{\Delta_{pd}} \cong -\frac{C}{\exp(qx)} = -p \exp(-qx), \quad (27g)$$

where t_{dd} has been found to be insensitive to the weight w, but Δ_{pd} is largely variable with the computational methods, leading to the above approximation. These fitting parameters are summarized in Table V. The fitting procedures are not so precise but are useful for qualitative understanding of general behaviors of chemical indices by the hybrid DFT methods. These procedures are applicable to other orbitals in Tables I through IV.

Model 1 (1a) and Model 3 (2a)

For the model 1 (**1a**), the NOs denoted by numbers 165, 166, and 167 correspond to p-type orbitals, p_x (σ_L: b_1), p_y (π_{2L}: b_2), and p_z (π_{1L}: a_1), respectively. The occupation numbers of these orbitals are nearly 2.0, and these orbitals are doubly occupied natural orbitals (DONOs) mainly extending over the μ-oxo atom. The upper NOs labeled by 168, 169, 170, 171, and 172 are the bonding orbitals with σ (a_1), π_1 (b_1), π_2 (a_2), δ_1 (a_1), and δ_2 (a_2) symmetries, respectively. The occupation numbers of these orbitals, which

TABLE III

Chemical indices of the NOs for Hr model compound 3 (2a).[a]

Methods	Orbital interaction	b	I	B	Y	Q	U
UHF	σ	0.0843	0.0633	0.1673	0.8327	0.9964	0.9929
	$\pi1$	0.0702	0.0524	0.1397	0.8603	0.9975	0.9951
	$\pi2$	0.0570	0.0422	0.1135	0.8865	0.9984	0.9968
	$\delta1$	0.0077	0.0056	0.0153	0.9847	1.0000	0.9999
	$\delta2$	0.0057	0.0041	0.0114	0.9886	1.0000	1.0000
UBHandHLYP	σ	0.1793	0.1403	0.3475	0.6525	0.9838	0.9678
	$\pi1$	0.1610	0.1250	0.3138	0.6862	0.9870	0.9741
	$\pi2$	0.1361	0.1046	0.2673	0.7327	0.9907	0.9815
	$\delta1$	0.0217	0.0158	0.0434	0.9566	0.9998	0.9995
	$\delta2$	0.0159	0.0116	0.0319	0.9681	0.9999	0.9997
UB3LYP	σ	0.3282	0.2719	0.5926	0.4074	0.9446	0.8923
	$\pi1$	0.3081	0.2534	0.5628	0.4372	0.9514	0.9051
	$\pi2$	0.2317	0.1852	0.4398	0.5602	0.9728	0.9463
	$\delta1$	0.0501	0.0370	0.1000	0.9000	0.9987	0.9975
	$\delta2$	0.0311	0.0228	0.0621	0.9379	0.9995	0.9990
UBLYP	σ	0.7748	0.7344	0.9683	0.0317	0.6322	0.3997
	$\pi1$	0.7454	0.7013	0.9583	0.0417	0.6666	0.4444
	$\pi2$	0.3769	0.3177	0.6601	0.3399	0.9262	0.8579
	$\delta1$	0.1075	0.0816	0.2126	0.7874	0.9942	0.9884
	$\delta2$	0.0474	0.0350	0.0946	0.9054	0.9989	0.9978

[a] Antiferromagnetic spin state.

are equal to $1.0 + b$ values (b: effective bond order), are larger than 1.0. Here these orbitals are referred to as the highly occupied natural orbitals (HONOs).

Table I summarizes the occupation numbers of HONOs with each symmetry. The more upper NOs 173, 174, 175, 176, and 177 are the antibonding

TABLE IV

Chemical indices of the NOs for Hr model compound 4 (2b).[a]

Methods	Orbital interaction	b	I	B	Y	Q	U
UHF	σ	0.0287	0.0210	0.0573	0.9427	0.9996	0.9992
	$\pi2$	0.0149	0.0108	0.0297	0.9703	0.9999	0.9998
	$\pi1$	0.0104	0.0075	0.0208	0.9792	0.9999	0.9999
	$\delta1$	0.0025	0.0018	0.0051	0.9949	1.0000	1.0000
UBHandHLYP	σ	0.0576	0.0427	0.1148	0.8852	0.9983	0.9967
	$\pi2$	0.0318	0.0233	0.0635	0.9365	0.9995	0.9990
	$\pi1$	0.0191	0.0139	0.0382	0.9618	0.9998	0.9996
	$\delta1$	0.0060	0.0043	0.0120	0.9880	1.0000	1.0000
UB3LYP	σ	0.1107	0.0841	0.2187	0.7813	0.9939	0.9877
	$\pi2$	0.0643	0.0478	0.1280	0.8720	0.9979	0.9959
	$\pi1$	0.0364	0.0267	0.0726	0.9274	0.9993	0.9987
	$\delta1$	0.0123	0.0089	0.0247	0.9753	0.9999	0.9998
UBLYP	σ	0.2526	0.2035	0.4748	0.5252	0.9676	0.9362
	$\pi2$	0.1439	0.1110	0.2820	0.7180	0.9896	0.9793
	$\pi1$	0.1072	0.0813	0.2119	0.7881	0.9942	0.9885
	$\delta1$	0.0143	0.0104	0.0285	0.9715	0.9999	0.9998

[a] Antiferromagnetic spin state.

orbitals with δ_2^* (b_2), δ_1^* (b_1), π_2^* (b_2), π_1^* (a_1), and σ^* (b_1) symmetries, respectively, which are referred to as lower unoccupied natural orbitals (LUNOs). Judging from the order of occupation numbers in HONOs, the orbital interactions become weaker in the order of σ, π_1, π_2, δ_1, and δ_2. These qualitative tendencies are independent from the hybrid DFT parameterizations.

The occupation numbers of δ_1 and δ_2 are almost 1.0 and are smaller than those of σ, π-type orbitals. From shapes of NOs in Figure 7a, these orbitals do not interact through μ-oxo. Alternately, δ_1-type interaction is through π orbital over carbonyl group of acetic acids and δ_2-type interaction is through orbitals that make ligands field as lone pair from oxygen atoms in carbonyl groups and nitrogen atoms in HBpz$_3$. All the NOs for **1a** are shown in Figure 7a.

The DONOs 149, 150, and 151 for the model 3 (**2a**) correspond to p_y (π_{2L}: b_2), p_x (σ_L: b_1), and p_z (π_{1L}: a_1), respectively. The order of HONOs and LUNOs are the same as model 1 (**1a**). In the natural orbital (NO = 157) coordinations of lone pair orbitals of nitrogen atoms of Me$_3$TACN and oxygen atoms of carbonyl groups to iron center are found. The NOs of **2a** are omitted here.

Model 2 (1b) and Model 4 (2b): Protonated Models

Model 2 (**1b**) is generated from protonation of model 1 (**1a**). In **1b**, DONOs corresponding to p_y (π_{2L}: b_2), p_x (σ_L: b_1), and p_z (π_{1L}: a_1) in **1a** are not found in the lower NOs, labeled as 165, 166, and 167. They are delocalized over [Fe$_2$O(OOCR$_2$)$_2$] cores. From Table II, HONOs are σ (a_1), π_2 (a_2), δ_1 (a_1), δ_2 (a_2), and π_1 (b_1) in the order of occupation numbers. The LUNOs are π_1^*(a_1), δ_2^* (b_2), δ_1^* (b_1), π_2^*

TABLE V

Fitting parameters of chemical indices with the weight of the HF exchange potential.

Chemical indices	p	$-q$	R[a]
b	0.607	2.017	0.965
l	0.546	2.219	0.959
B	0.620	2.345	0.981
Y	0.620	2.345	0.981
Q	0.757	3.885	0.998
U	0.757	3.902	0.999

[a] Standard deviation.

165(DO) 166(DO) 167(DO) 168(σ)
169(π_1) 170(π_2) 171(δ_1) 172(δ_2)
173(δ_2^*) 174(δ_1^*) 175(π_2^*) 176(π_1^*)
177(σ^*)

(a)

165(DO) 166(DO) 167(DO) 168(σ)
169(π_2) 170(δ_1) 171(δ_1) 172(π_1)
173(π_1^*) 174(δ_2^*) 175(δ_1^*) 176(π_2^*)
177(σ^*)

(b)

150(DO) 151(DO) 152(DO,δ_1) 153(DO,δ_1^*)
154(σ) 155(π_2) 156(π_1) 157(δ_2)
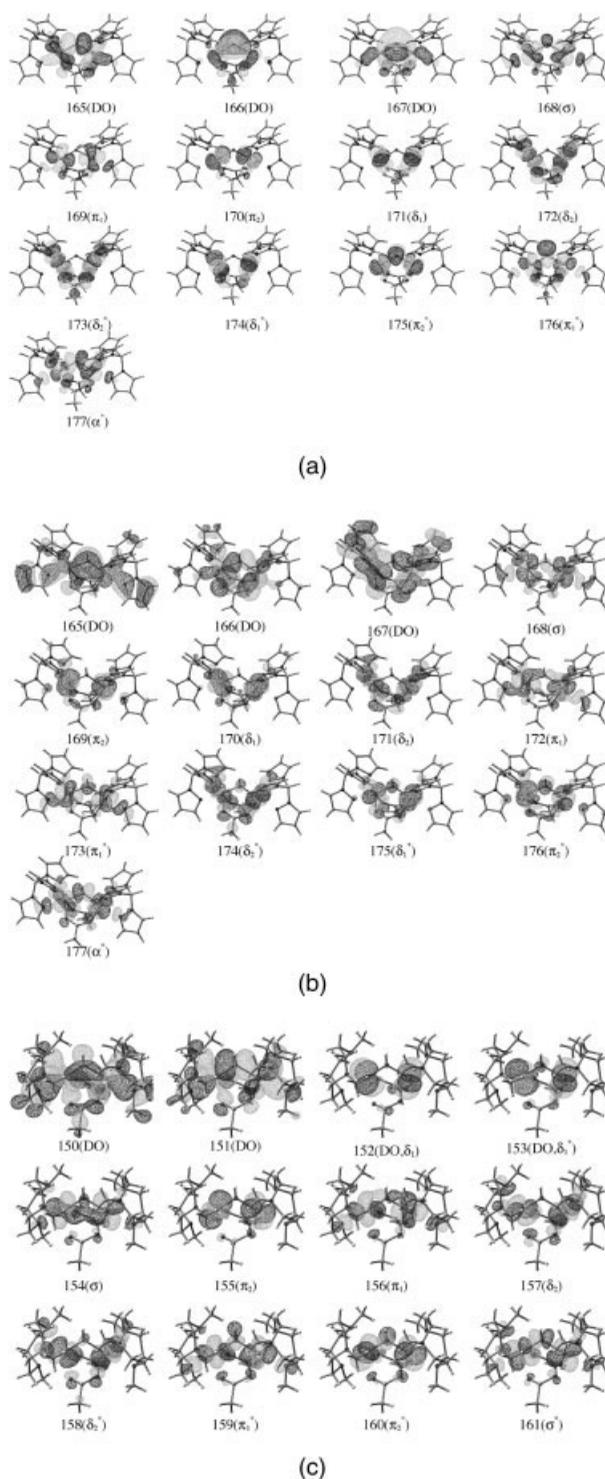158(δ_2^*) 159(π_1^*) 160(π_2^*) 161(σ^*)

(c)

FIGURE 7. Natural orbitals for Hemerythrin model compounds in antiferromagnetic spin state by UB3LYP/MIDI+P+-6-31G*: (a) **1a**, (b) **1b**, and (c) **2b** (see Fig. 5). The symmetries of the natural orbitals are given in Figure 6.

(b_2), and σ^* (b_1), respectively. These NOs are shown in Figure 7b.

Model 4 (**2b**) is generated from model 3 (**2a**) with protonation and two-electron reduction. The NOs 152 and 153 are the closed-shell orbitals formed by the two-electron reductions and correspond to δ_1 (a_1) and δ_1^* (b_1), respectively. These orbitals do not interact with the ligands. If a dioxygen molecule is coordinating to the iron, this iron orbital can interact with π^* orbital of dioxygen. The upper DONOs 150 and 151 correspond to p_y (π_{2L}: $\underline{b}_2$) and p_x (σ_L: b_1). The HONOs are σ (a_1), π_2 (a_2), δ_1 (a_1), π_1 (b_1), and δ_2 (a_2), in order of occupation numbers. These NOs are shown in Figure 7c. The bonding character of π_1 in model 4 (**2b**) becomes weaker in the case of model 2 (**1b**).

It should be noted that π_1 orbital interaction becomes weak by protonation over μ-oxo. The orbital associated with the protonation is p_z. This p_z is the mediating orbital for π_1 superexchange orbital interaction. The p_z component is found in LUNO (NO = 173) in model 2 (**1b**) and in LUNO (NO = 159) in model 4 (**2b**), and protons are in contact only with the p_z orbital in **1b** and in **2b**. In consequence, p_z lone pair orbital in model 1 (**1a**) or model 3 (**2a**) is protonated in **1b** or **2b**, and the resulting orbital interaction through p_z is in turn weakened. Although two-electron reduction occurs in addition to the protonation in model 3 (**2a**), the change of π_1 interaction in **2b** is the same as in model 1 (**1a**).

CHEMICAL INDICES

Chemical indices (b, I, B, Y and Q, and U) defined in the fourth section are calculated by the four computational methods: UHF, UBHandHLYP, UB3LYP, and UBLYP. The effective bond order (b) and information (I) values are the bond indices for BS solutions, whereas the effective bond order (B) and diradical character ($Y = 1 - B$) values are chemical indices after spin projection. The B value is regarded as spin-projected b value. The Q and U indices are useful for pictorial understanding of populations of unpaired electrons. The functional behaviors of these indices with $w(x)$ are given in Eq. (27). Here, several characteristic features for **1a–2b** are discussed on the basis of the numerical results.

The b and B values of the diiron complexes increase in the order: UHF, UBHandHLYP, UB3LYP and UBLYP. For instance, the $b(B)$-values for σ-orbital in model 1 (**1a**) are 0.09 (0.18), 0.19 (0.37), 0.34 (0.61), and 0.76 (0.96), respectively, as summarized in Table I. The information entropy I_n also exhibits

similar behavior. Variations of b, B, and I_n by the HDFT methods are quite large, as shown in Tables I through IV. Therefore, we must examine the reliability of the computational methods in comparison with the experimental results or in accord with the theoretical procedure (see below). As shown in the next section, the effective exchange integrals (J) by UB3LYP method is consistent with the observed values. Then UB3LYP is found to be the most reliable for **1a–2b**. For this reason, b and B values by UB3LYP are used for further discussions on bond indices. In the protonated model 2 (**1b**), $b(B)$-values for σ, π_2, δ_1, δ_2, and $\underline{\pi}_1$ interactions are 0.17 (0.34), 0.06 (0.13), 0.05 (0.10), 0.05 (0.10), and 0.04 (0.07), respectively, as shown in Table II. Particularly, $b(B)$-value of π_1 is decreased significantly by the protonation, whereas the $b(B)$-values of σ and π_2 are decreased by nearly one half. There is only negligible variation in $b(B)$-values of δ orbitals.

In model 3 (**2a**) $b(B)$-values for σ, π_1, π_2, δ_1, and δ_2 interactions are 0.33 (0.59), 0.31 (0.56), 0.23 (0.44), 0.05 (0.10), and 0.03 (0.06), respectively. This result shows that σ and π orbital interactions through μ-oxo are fairly stronger than δ orbital interaction through acetate groups. In model 4 (**2b**), and b and B values for σ, π_2, δ_1, and $\underline{\pi}_1$ interactions are 0.11 (0.22), 0.06 (0.13), 0.04 (0.07), and 0.01 (0.02), respectively. After the protonation, $b(B)$ value of π_1 is also decreased significantly, and the $b(B)$ values of σ and π_2 are decreased by nearly one third. It is concluded that superexchange interaction via π_1 decreases significantly by the protonation on μ-oxo, accompanied by the decrease of superexchange interactions via σ and π_2. These cooperated reductions in σ and π superexchange interactions may be attributed to the elongation of the Fe—O bond length by protonation.

EFFECTIVE EXCHANGE INTEGRALS

The effective exchange integrals (J) for **1a–2b** are calculated by four computational methods: UHF, UBHandHLYP, UB3LYP, and UBLYP. Because the calculated $J^{(1)}$ and $J^{(3)}$ values are not very different, these species are regarded as typical, strong electron correlation systems. Therefore, the calculated $J^{(3)}$ values are plotted against the weight ($w = x$) of the HF exchange potentials as shown in Figure 8. As expected from Eq. (27g), we have performed two parameters fittings. The parameter sets (p, q) are determined as (321, 3.202), (55.3, 4.208), (302, 3.199), and (39.5, 2.494) for **1a**, **1b**, **2a**, and **2b**, re-
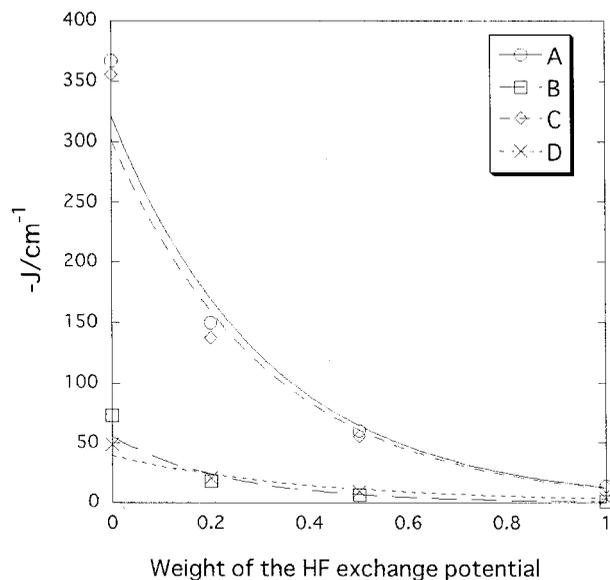
FIGURE 8. Variations of the effective exchange integrals ($-J_{ab}$) for diiron complexes A (**1a**), B (**1b**), C (**2a**), and D (**2b**) with change of the mixing parameter w of the HF exchange potential in the HDFT method.

spectively. Because the experimental J values are in the ranges $-115 \sim -135$ cm^{-1} for **1a** and **2a** and $-10 \sim -20$ cm^{-1} for **1b** and **2b**, the optimized w-values are larger than 20% but smaller than 50%. In fact, they are about 31%, 28%, 29%, and 45% for **1a**, **1b**, **2a**, and **2b**, respectively, if the experimental J-values are used for estimation. This in turn means that UB3LYP ($w = 20\%$) is one of the most useful hybrid DFT methods for estimations of J-values for **1a**, **1b**, and **2a**, whereas UBHandHLYP ($w = 50\%$) is useful for **2b**. It is noteworthy that **2b** involves the divalent iron Fe(II), although **1a**, **1b**, and **2a** have trivalent iron Fe(III). Instead of reoptimizations of w [58], here we used J-values by UB3LYP for further characterizations and discussions of **1a–2b**.

In model 1 (**1a**) J-values by UB3LYP are $J^{(1)} = -151.70$ cm^{-1}, $J^{(2)} = -126.42$ cm^{-1}, and $J^{(3)} = -149.97$ cm^{-1} in comparison with experimental $J^{\text{exp}} = -121$ cm^{-1} value [31]. In model 2 (**1b**) the calculated J-values by UB3LYP are $J^{(1)} = 18.18$ cm^{-1}, $J^{(2)} = -15.15$ cm^{-1}, and $J^{(3)} = -18.15$ cm^{-1} in comparison with experimental $J^{\text{exp}} = -17$ cm^{-1} value [15]. In model 3 (**2a**) the calculated J-values by UB3LYP are $J^{(1)} = -138.85$ cm^{-1}, $J^{(2)} = -115.71$ cm^{-1} and $J^{(3)} = -137.4$ cm^{-1} in comparison with experimental $J^{\text{exp}} = -119$ cm^{-1} value [6]. In model 4 (**2b**) the calculated J-values by UB3LYP are $J^{(1)} = -20.67$ cm^{-1}, $J^{(2)} = -16.54$ cm^{-1}, and $J^{(3)} = -20.65$

cm^{-1} in comparison with experimental $J^{\text{exp}} = -13$ cm^{-1} value [6].

From these results J-values by UB3LYP are in qualitative agreement with experimental values. The UHF predicts smaller J-values than experimental J values, whereas DFT indicates the reverse tendency. Therefore, hybrid DFT, such as UBHandHLYP and UB3LYP, tends to reproduce the experimental J-values. This means that appropriate evaluation of U_{dd} in Eq. (23) is crucial for strong electron correlation systems; note that U_{dd} is related to Δ_{pd} in Eq. (4). In this paper, we do not investigate theoretical procedures to estimate the weight (w) of the HF exchange potential. Because UHF solutions are uniquely determined for **1a–2b**, chemical indices by UHF are calculated by using the occupation numbers of UHF NO(UNO). Therefore they can be used to diagnose w in the HDFT. For example, B3LYP is preferable for systems with the intermediate electron correlation, whereas UBHandHLYP, such as UB2LYP, is inevitable for strongly correlated electron systems. Hybrid DFT, LDA+U and related theories are practical and handy methods for the purpose. However, more nonempirical methods such as multireference DFT and related density-matrix theories [59, 60] are desirable for improvements of the computational procedures in this field.

Discussions and Conclusion

ANTIFERROMAGNETIC EXCHANGE INTERACTIONS

Spin–spin coupling in diiron complexes is usually well described by the isotropic spin-exchange Hamiltonian in Eq. (1). Kurtz [3] summarized a lot of effective exchange integrals (J_{ab}) for diiron cores Fe(III)(OFe(III) in inorganic and bioinorganic complexes. The J_{ab}-values for the majority of oxo-bridged diiron (III) complexes is in the range -80 to -120 cm^{-1}. The experimental J_{ab}-values for **1a** and **2a** are consistent with the general tendency, and their calculated J_{ab}-values by UB3LYP are also in good agreement with the experiments. On the other hand, magnetic observations show that the J_{ab}-values for (μ-hydroxo) diiron complexes are reduced to -10 to -20 cm^{-1}. The experimental and calculated J_{ab}-values for **1b** and **2b** are compatible with the general trend. This in turn indicates that spin-polarized hybrid DFT (HUDFT), UB3LYP, is a useful and practical method for theoretical investiga-
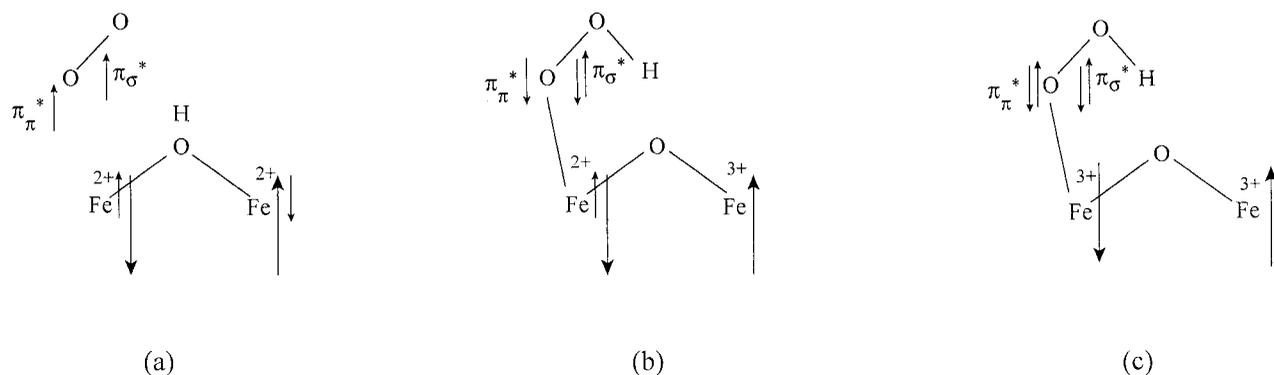
FIGURE 9. Reversible dioxygen binding mechanism of Hr. Two one-electron transfer mechanism indicated by spectroscopy and DFT (Ref. [62]): (a) deoxyHr, (b) one-electron transfer from Fe1 to O_2 coupled with tunneling of the hydroperoxide proton to the μ-oxo bridge, (c) oxyHr.

tion of the electronic structures of diiron cores in metalloenzymes.

RELATION TO OTHER THEORETICAL STUDIES

Theoretical studies of magnetic interactions in model 1 (**1a**) and model 2 (**1b**) were reported by Rodriguez and McCusker [61]. The authors reported that the calculated $J = -305.4$ cm^{-1} for **1a** and $J = -46.6$ cm^{-1} for **1b** at UBPW91/6-311G*// UB3LYP/6-31G* [J are converted to the definition of Eq. (1)]. The magnitudes of their J-values are consistent with those of the pure DFT methods, such as BLYP, and are much larger than the corresponding experimental values. Their overestimation of J-values also support that diiron cores under discussion belongs to the intermediary electron-correlation system. The authors also concluded that the strength of each orbital interaction can be estimated by the overlap of the natural magnetic orbitals in the BS state, discussed in the second section. The strongest interaction in model 1 (**1a**) was reported as π_2 through μ-oxo. This result is different from our conclusions on the basis of the NO analysis followed by chemical indices calculations.

SPIN, CHARGE, AND ORBITAL CONTROLS OF DIOXYGEN BONDING IN HR

Here we consider relationships between magnetism and chemical bonds. The stepwise one-electron transfer from diiron to molecular oxygen is considered to be essential in the oxygenation process of Hr. This oxygenation should proceed with

the intersystem crossing, because oxyHr is singlet but molecular oxygen is triplet in the ground state. The weak antiferromagnetic interactions between Fe ions through hydroxo are preferable to the intersystem crossing because of the low energy gaps among each spin state. The strong antiferromagnetic interactions through oxo bridge between diiron centers are realized after the electron transfer from Fe(II) to O_2. Thus, magnetism is an important viewpoint for the oxygen bonding in Hr and related species.

The dioxygen bonding mechanism in Hr has already been studied using DFT calculations [62]. From the results, the coupling mechanism of electron transfer (ET) and proton transfer (PT) is proposed. The dioxygen bonding mechanism is composed of two-step ETs as illustrated in Figure 9. In the first step, one-electron transfer from distal iron to bonding oxygen and PT from hydroxy to peroxide by tunneling occur at the same time (ET-PT). The σ bond is formed between iron and oxygen of hydroperoxide. In the second step, one-electron transfer occurs from proximal iron to π^* orbital at hydroperoxide for the shot bond length by the formation of σ bond. The π bond is formed between iron and oxygen of hydroperoxide. In the first step of the oxygen bonding process the ET path and proton tunneling uses the π_1 orbital interaction between diirons. This interaction orbital contributes to σ orbital formation with dioxygen. In the second step, one-electron transfer occurs from the δ orbital to hydroperoxide. From our calculations the δ interactions were weak compared with σ, π interactions and these δ orbitals are localized in each iron

site. The localizing δ orbital spreads out toward vertical direction to μ-oxo, and it is effective to interact with π^* orbital of hydroperoxide. Orbitals freedom and their symmetry are deeply related to the oxygen bonding mechanism.

From the accumulated theoretical and experimental results [1, 2, 60], spin, charge, and orbital freedoms play important roles for trapping of molecular oxygen in diiron cores. Spin is responsible for electron localization on diiron, which permits the one-electron oxidation-reduction process, that is, one-electron transfer, and orbital freedom is important for active control of multistep ET processes: different orbitals (π, δ, etc.) play different roles in several oxidation-reduction steps. Probably, protein dynamics will control overall processes as effective reason fields, as illustrated in Figure 10. This is a common characteristic of strong or intermediary electron correlation systems in material and biological sciences [21].

CONCLUDING REMARKS

The superexchange interaction in diiron cores in Hr and related model complexes (**1a–2b**) is not direct orbital interactions between spin sites (direct exchange interaction) but interaction through bridging ligands (O^{2-} or OH^-) between Fe-ion sites. The BS hybrid DFT (HDFT) calculations of **1a–2b** are not time-consuming compared with the CAS-SCF followed by the perturbation corrections. The NO analysis of BS HDFT solutions provides the SA orbitals and their occupation numbers, which are used to calculate several chemical indices such as effective bond order, information entropy, diradical character, and unpaired electron density. They are defined by the occupation numbers of
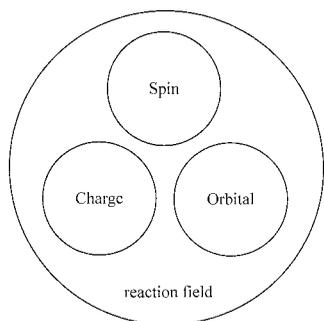

FIGURE 10. Active controls of spin, charge, and orbital freedoms in diiron cores in metalloenzymes by reaction field such as ligand and protein.
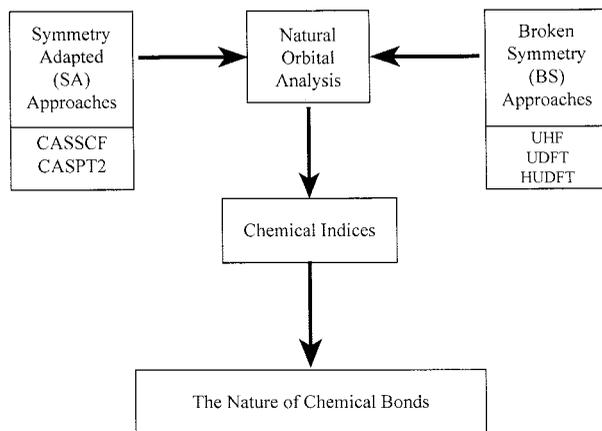

FIGURE 11. Theoretical scheme for elucidation of the nature of chemical bonds by chemical indices defined by the occupation numbers of NOs by the SA method and BS method with and without spin projection.

NOs before and after spin projections. The chemical indices are equally applicable to NOs by CAS-SCF and various CIs. Therefore, these are interfaces between BS DFT and SA CAS-SCF (CI).

In Hr and its model compounds **1a–2b**, magnetic interactions change dramatically by oxo environment. Hemerythrin must use this change artfully. Using Hr model compounds, HDFT calculations are performed for the elucidation of the magnetic interactions governing in these systems. The effective exchange integral (J) values are decreased to a different order of magnitude by protonation of μ-oxo. These calculated J-values are in good agreement with experimental values from magnetic susceptibility measurements. The superexchange interactions through μ-oxo are strong. By protonation (from z direction) of μ-oxo, π_1 orbital interactions performed through p_z orbital on μ-oxo especially decreased. The p_z orbital stabilization by protonation is one reason for the decrease of interactions.

In conclusion, the nature of chemical bonds in diiron cores in metalloenzymes can be systematically grasped by the Hubbard model, intermolecular CI, and spin-polarized hybrid DFT calculations, followed by the NO analysis and resulting chemical indices. Figure 11 illustrates our theoretical scheme for theoretical investigation of chemical bonds in metalloenzymes. We did not discuss physical foundations of the BS methods [21, 63, 64] for theoretical investigations of strongly correlated electron systems. They are out of primary concern in this paper, because electronic structures of diiron cores are our main interest. The methods presented here will be

applied to other transition-metal complexes in enzymes.

References

1. Eklund, H. Handbook of Metalloproteins; Wiley: New York, 699–711.

2. Lippard, S. J.; Berg, J. M. Principles of Bioinorganic Chemistry; University Science Books: California, 1994.

3. Kurtz, D. M., Jr. Chem Rev 1990, 90, 585.

4. Que, L., Jr.; True, A. E. Bioinorg Chem 1990, 38, 97.

5. Armstrong, W. H.; Lippard, S. J. J Am Chem Soc 1983, 105, 4837.

6. Hartman, J. R.; Rardin, R. L.; Chaudhuri, P.; Pohl, K.; Wieghardt, K.; Nuber, B.; Weiss, J.; Papaefthymiou, G. C.; Frankel, R. B.; Lippard, S. J. J Am Chem Soc 1987, 109, 7387.

7. Loehr, J. S.; Wheeler, W. D.; Shiemke, A. K.; Averill, B. A.; Loehr, T. M. J Am Chem Soc 1989, 111, 8084.

8. Spool, A.; Williams, I. D.; Lippard, S. J. Inorg Chem 2156, 24, 2156.

9. Zhang, K.; Stern, E. A.; Ellis, F.; Loehr, J. S.; Shiemke, A. K. Biochemistry 1988, 27, 7470.

10. Ericson, A.; Hedman, B.; Hodgson, K. O. J Am Chem Soc 1988, 110, 2332.

11. Scarrow, R. C.; Maroney, M. J.; Palmer, S. M.; Que, L. J Am Chem Soc 1986, 108, 6832.

12. Scarrow, R. C.; Maroney, M. J.; Palmer, S. M.; Que, L.; Roe, A. L.; Saloew, S. P.; Stubbe, J. J Am Chem Soc 1987, 109, 7857.

13. Czernuszewics, R. S.; Sheats, J. E.; Spiro, T. G. Inorg Chem 1987, 26, 2063.

14. Hadman, B.; Co, M. S.; Armstrong, W. H.; Hodgson, K. O.; Lippard, S. J. Inorg Chem 1986, 25, 3708.

15. Kauzlarich, S. M.; Teo, B. K.; Zirino, T.; Burman, S.; Davis, J. C.; Averill, B. A. Inorg Chem 1986, 25, 2781.

16. Armstrong, W. H.; Lippard, S. J. J Am Chem Soc 1984, 106, 4632.

17. Turowski, P. N.; Armstrong, W. H.; Liu, S.; Brown, S. N.; Lippard, S. J. Inorg Chem 1994, 33, 636.

18. Kitajima, N.; Tamura, N.; Amagai, H.; Fukui, H.; Moro-oka, Y.; Mizutani, Y.; Kitagawa, T.; Mathur, R.; Heerwegh, K.; Reed, C. A.; Randall, C. R.; Que, L. J.; Tatsumi, K. J Am Chem Soc 1994, 116, 9071.

19. Olafson, B. D.; Goddard, W. A., III. Proc Natl Acad Sci USA 1977, 72, 1335.

20. Takano, Y.; Kubo, S.; Onishi, T.; Isobe, H.; Yoshioka, Y.; Yamaguchi, K. Chem Phys Lett 2001, 355, 395–403.

21. Yamaguchi, K. In Self-Consistent Field: Theory and Applications; Carbo, R.; Klobukowski, M., Eds.; Elsevier Scientific Publishers: Amsterdam, Oxford, New York, Tokyo, 1990; p 727.

22. Yamaguchi, K.; Yabushita, S.; Fueno, T. J Chem Phys 1979, 71, 2321.

23. Yamaguchi, K. J Mol Structure 1983, 103, 101.

24. Yamaguchi, K.; Takahara, Y.; Fueno, T. In Applied Quantum Chemistry; Smith, V. H., Jr.; Schaefer, H. F., III; Morokuma, K.; Reidel, S. Kluwer Academic Publishers: Dordrecht, 1986; p 155.

25. Yamaguchi, K.; Takada, K.; Otsuji, Y.; Mizuno, K. in Organic Peroxides, edited by W. Ando, John Wiley & Sons, 1992, p 1.

26. Yamaguchi, K.; Yabushita, S.; Fueno, T.; Kato, S.; Morokuma, K.; Iwata, S. Chem Phys Lett 1980, 71, 563.

27. Koizumi, K.; Shoji, M.; Nishiyama, Y.; Maruno, Y.; Kitagawa, Y.; Soda, K.; Yamanaka, S.; Okumura, M.; Yamaguchi, K. Int J Quantum Chem 2004, 100, in press.

28. Yamaguchi, K.; Nakano, M.; Namimoto, N.; Fueno, T. Jpn J Appl Phys 1988, 27, L1835.

29. Yamaguchi, K. Int J Quantum Chem 1990, 37, 167.

30. Yamaguchi, K.; Yamaki, D.; Kitagawa, Y.; Takahata, M.; Kawakami, T.; Ohsaku, T.; Nagao, H. Int J Quantum Chem 2003, 92, 47.

31. Kawakami, T.; Taniguchi, T.; Kitagawa, Y.; Takano, Y.; Nagao, H.; Yamaguchi, K. Mol Phys 2002, 100, 2641.

32. Kawakami, T.; Taniguchi, T.; Nakano, S.; Kitagawa, Y.; Yamaguchi, K. Polyhedron 2003, 22, 2051.

33. Nakano, S.; Kitagawa, Y.; Kawakami, T.; Yamaguchi, K. Polyhedron 2003, 22, 2027–2038.

34. Imada, M.; Fujimori, A.; Tokura, Y. Rev Mod Phys 1998, 70, 1040.

35. Yamaguchi, K. Chem Phys Lett 1979, 68, 477.

36. Yamaguchi, K. Chem Phys Lett 1975, 33, 330.

37. Yamaguchi, K. Chem Phys Lett 1975, 35(2), 230.

38. Isobe, H.; Takano, Y.; Kitagawa, Y.; Kawakami, T.; Yamanaka, S.; Yamaguchi, K.; Houk, K. N. Mol Phys 2002, 100, 717–727.

39. Isobe, H.; Takano, Y.; Kitagawa, Y.; Kawakami, T.; Yamanaka, S.; Yamaguchi, K.; Houk, K. N. J Phys Chem A 2003, 107(5), 682.

40. Becke, A. D. J Chem Phys 1993, 98, 5648.

41. Beck, A. D. Phys Rev A 1988, 38, 3098.

42. Lee, C.; Yang, W.; Parr, R. G. Phys Rev B 1988, 37, 785.

43. Frisch, M. J.; Trucks, G. W.; Schlegel, H. B.; Scuseria, G. E.; Robb, M. A.; Cheeseman, J. R.; Zakrzewski, V. G.; Montgomery, J. A., Jr.; Stratmann, R. E.; Burant, J. C.; Dapprich, S.; Millam, J. M.; Daniels, A. D.; Kudin, K. N.; Strain, M. C.; Farkas, O.; Tomasi, J.; Barone, V.; Cossi, M.; Cammi, R.; Mennucci, B.; Pomelli, C.; Adamo, C.; Clifford, S.; Ochterski, J.; Petersson, G. A.; Ayala, P. Y.; Cui, Q.; Morokuma, K.; Rega, N.; Salvador, P.; Dannenberg, J. J.; Malick, D. K.; Rabuck, A. D.; Raghavachari, K.; Foresman, J. B.; Cioslowski, J.; Ortiz, J. V.; Baboul, A. G.; Stefanov, B. B.; Liu, G.; Liashenko, A.; Piskorz, P.; Komaromi, I.; Gomperts, R.; Martin, R. L.; Fox, D. J.; Keith, T.; Al-Laham, M. A.; Peng, C. Y.;

Nanayakkara, A.; Challacombe, M.; Gill, P. M. W.; Johnson, B.; Chen, W.; Wong, M. W.; Andres, J. L.; Gonzalez, C.; Head-Gordon, M.; Replogle, E. S.; Pople, J. A. Gaussian, 98, Revision A.11.3; Gaussian: Pittsburgh, 2002.

44. Hariharan, P. C.; Pople, J. A. Theo Chem Acta 1973, 28, 213.

45. Hehre, W. J.; Ditchdield, R.; Pople, J. A. J Chem Phys 1972, 56, 2257.

46. Huzinaga, S. Gaussian Basis Sets for Molecular Calculations; Elsevier: Amsterdam, Oxford, New York, Tokyo, 1984.

47. Hay, P. J. J Chem Phys 1977, 66, 4377.

48. Han, W. G.; Lovell, T.; Liu, T.; Noodleman, L. Inorg Chem 2003, 42, 2751.

49. Noodleman, L.; Case, D. A. Adv Inorg Chem 1992, 38, 423.

50. Ginsberg, A. P. J Am Chem Soc 1980, 102, 111.

51. Bencini, A.; Totti, F.; Daul, C. A.; Doclo, K.; Fantucci, P.; Barone, V. Inorg Chem 1997, 36, 5022.

52. Yamaguchi, K.; Fukui, H.; Fueno, T. Chem Lett 1986, 625.

53. Yamaguchi, K.; Tsunekawa, T.; Toyoda, Y.; Fueno, T. Chem Phys Lett 1988, 143, 371.

54. 3D Search and Research using the Cambridge Structural Database. Allen, F. H., Kennard, O. Chemical Design Automation News 1993, 8, 31–37.

55. Armstrong, Q. H.; Spool, A.; Papaefthymiou, G. C.; Frankel, R. B.; Lippard, S. J. J Am Chem Soc 1984, 106, 3653.

56. Cohen, J. D.; Payne, S.; Hagen, K. S.; Sanders-Loehr, J. J Am Chem Soc 1997, 119, 2960.

57. Lachicotte, R.; Kitaygorodskiy, A.; Hagen, K. S. J Am Chem Soc 1993, 115, 8883.

58. Kitagawa, Y.; Soda, T.; Shigeta, Y.; Yamanaka, S.; Yoshioka, Y.; Yamaguchi, K. Int J Quantum Chem 2001, 84, 592.

59. Miehlich, B.; Savin, A.; Stoll, H.; Preuss, H. Chem Phys Lett 1989, 159, 200.

60. Takeda, R.; Yamanaka, S.; Yamaguchi, K. Chem Phys Lett 2002, 366, 321.

61. Rodriguez, J. H.; McCusker, J. K. J Chem Phys 2002, 116, 6253.

62. Brunold, T. C.; Solomon, E. I. J Am Chem Soc 1999, 121, 8288.

63. Yamaguchi, K. Chem Phys 1978, 29, 117.

64. Takatsuka, K.; Yamaguchi, K.; Fueno, T. Theoret Chim Acta 1978, 48, 175.